# Transonic Navier-Stokes Solutions for a Fighter-Like Configuration

Jolen Flores,* Steven G. Reznick,† Terry L. Holst,‡ and Karen Gundy§
*NASA Ames Research Center, Moffett Field, California*

**The transonic Navier-Stokes (TNS) wing code is extended to a 16-zone TNS wing/fuselage code and used to solve the transonic viscous flow over a modified F-16A. The computer code, called Transonic Navier-Stokes Wing/Fuselage (TNSWF), uses a zonal approach to solve the three-dimensional Euler and Navier-Stokes equations. With the zonal implementation, clustering suitable for viscous calculations is achieved on all solid surfaces. The transonic case has flow conditions of $M_\infty = 0.9$, $\alpha = 4.12$ deg, and a Reynolds number based on root chord of 4.5 million. This case required about 3000 iterations to reduce the L2 norm of the residual by these orders, which takes about 15 h of CPU time on the current NASA Ames computer. Pressure distributions, as well as separation patterns, compare favorably with experiment for this transonic case.**

## Nomenclature

$C_L$ = lift coefficient
$C_p$ = pressure coefficient
$M_\infty$ = freestream Mach number
$\alpha$ = angle of attack
$\xi, \eta, \zeta$ = transformed coordinate system

## Introduction

THE two primary tools at the disposal of the design aerodynamicist are wind-tunnel experiments and analytical methods. Although wind-tunnel experiments can handle complicated geometries, they are limited in flow conditions. Furthermore, both model fabrication and test time are expensive.[1] Analytical methods can yield fast, closed-form solutions, but they are limited to simple configurations. Computational fluid dynamics (CFD) is an alternative that has the potential to overcome the disadvantages associated with both wind-tunnel testing and analytical methods.

In the past, CFD has been useful in aircraft design but very limited in its scope. For example, if the flowfield did not contain shock waves or significant separation, the design of complex aircraft configurations was possible, using linear panel methods. If shock waves were present but vorticity and entropy production were not large, CFD was still a contributing factor in the design process through the use of the nonlinear potential methods. Still, with these limitations, CFD tools, coupled with optimizers, have been instrumental in the partial design or improvement of some simple aircraft. Some examples are the Rockwell forward-swept wing,[1] the HiMAT wing,[2] the Airbus A-310,[2] the Lockheed C-141B military transport,[2] and the Cessna Citation III business jet.[3]

Use of the time-accurate Navier-Stokes equations for transonic flow has not been fully exploited to date, having been primarily limited to simple-geometry, high-speed types of flows. These include Holst et al.,[4] Hung,[5,6] Shang,[7] and Pulliam and Steger.[8] More recently, a few transonic applications involving more sophisticated geometries have appeared, including those of Deiwert and Rothmund,[9] Deiwert et al.,[10] Fujii and Kutler,[11] and Mansour.[12] However, even those solutions were conducted on coarse grids and required large amounts of CPU time, which preclude their use for more complicated geometries.

The time is now at hand to demonstrate the power of CFD in the field of aircraft design and performance prediction. In particular, the solution of the more complete set of equations, that is, the Euler and Navier-Stokes equations, must be undertaken in response to the aircraft industry's demand for codes that can handle more complicated flowfields than are currently possible with successful linear or nonlinear potential methods. Examples of flowfields that logically require the Euler and Navier-Stokes formulation are associated with propulsion-airframe integration, store separation, multiple lifting surface interactions, high-angle-of-attack flowfield predictions, performance boundary predictions, and flutter and buffet calculations in which unsteady boundary-layer separation is present.

With the advent of supercomputers, it is now possible to solve the three-dimensional Euler and Navier-Stokes equations at reasonable computer costs. This is due to the fast vector processing available in these computers and to the improvement of existing CFD algorithms. To fully exploit the Euler and Navier-Stokes equations, however, high grid resolution is required. High grid resolution translates into large storage demands, which taxes even the supercomputers. To overcome ths storage problem, zonal approaches have become increasingly popular. Zonal approach means the partitioning of the flowfield into distinct "zones," each of which is solved independently. The zonal approach has a number of advantages. First, it mitigates the difficulty of generating three-dimensional grids for different types of complex configurations with appropriate clustering to capture high-gradient flow parameters; and it is this grid-generation difficulty that has probably been the single biggest reason for the slow development of three-dimensional CFD applications about complex geometries.[13]

Second, zonal methods allow different types of grid topologies to be used to improve mesh efficiency; that is, more points are used on the configuration where accuracy is desired, and fewer points are used away from the configuration where flow gradients are small. The zonal concept has been successfully applied to the full-potential equations[14,15] and to the Euler equations.[16,17] It is also possible with the zonal approach to solve different equation sets in different zones.[18]

The idea of solving the Euler and Navier-Stokes equations within the framework of zonal methods has been realized through the development of the TNS wing code. As a first

Presented as Paper 87-0032 at the AIAA 25th Aerospace Sciences Meeting, Reno, NV, Jan. 12-15, 1987; received Feb. 8, 1987; revision received May 1, 1987. 

*Research Scientist. Member AIAA.
†Major, USAF. Member AIAA.
‡Chief, Applied Computational Fluids Branch. Associate Fellow AIAA.
§Graduate Student. Student Member AIAA.

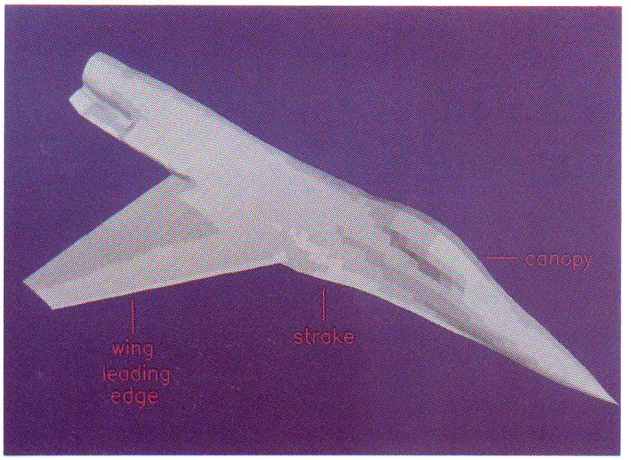


Fig. 1 F-16A modified geometry.

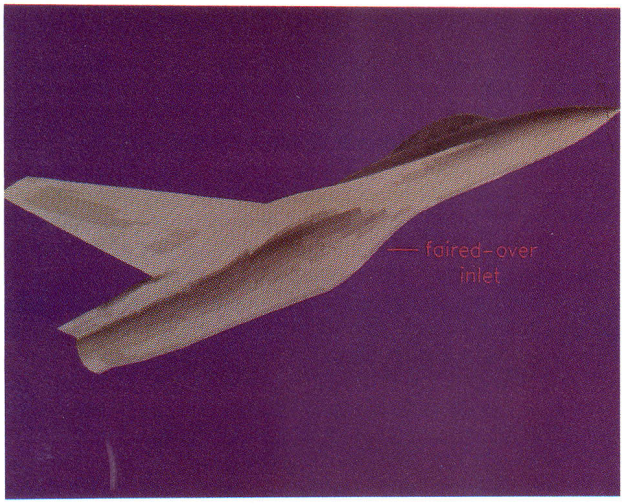


Fig. 2 F-16A modified geometry, highlighting the faired-over inlet.

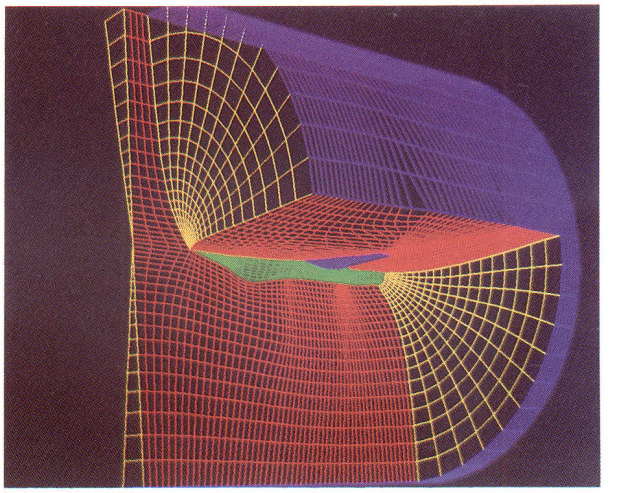

Fig. 3 Base grid about the F-16a geometry.

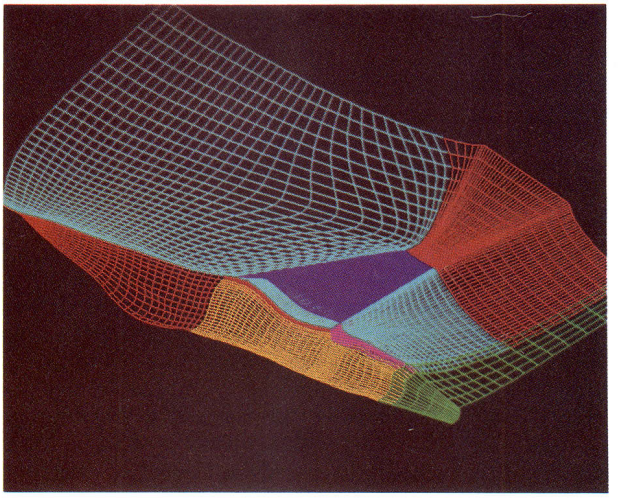

Fig. 4 Different zonal grids highlighted by colors.

step, the TNS code was developed to compute transonic flow over isolated arbitrary wing geometries with both free-air and wind-tunnel wall boundary conditions. For the wing code, the method utilized a zonal approach with a total of four grid zones. The Euler equations are solved in the two outer zones that surround the wing, and the thin-layer Navier-Stokes equations are solved in the two inner viscous zones on the airfoil surface. For a more thorough discussion of the algorithm, the zonal interfacing procedure, convergence rates, and the results of flows over different wings, the reader should consult Refs. 19–22.

The contribution of the current paper is the extension of the four-zone TNS wing code to a 16-zone TNS wing fuselage (TNSWF) code. In particular, the TNSWF code is used to solve transonic viscous flow over a modified F-16A. It should be mentioned that the combination of zonal methods and the solution of the Euler equations has been successful when used on complex geometries[23] and to solve the complete F-16A aircraft.[24] However, to the best of the authors' knowledge, this is the first successful implementation of the three-dimensional Euler and Navier-Stokes equations in a zonal approach for this type of complicated configuration.

## Zonal Philosophy

### F16A Geometry and Base Grid

The modified F-16A is shown in Fig. 1. Note that the forebody, canopy, leading-edge strake, wing, and shelf regions are unmodified. That is, the geometry is exactly that of the F-16A. The modified portion consists of the exclusion of the tail assembly and the fairing over of the inlet (Fig. 2). Achieving appropriate clustering at all solid boundaries for this complicated geometry is extremely difficult with a single grid. It is a manageable problem, however, when zonal methods are used. To initiate the TNSWF code, a base grid about the geometry is supplied as input. The base grid was generated by means of an elliptic method.[25] From Fig. 3, the topology about the fuselage can be seen. This polar grid collapses into a singular line in front of the fuselage nose but causes no problem in the flow solver because of the averaging about this singularity. A chordwise slice through the wing would reveal an H-mesh local topology.

### Description of Viscous-Inviscid Zones

The base grid is fed into the zonal routine, which subsequently creates 16 zones (by subdividing the original base grid). Through certain parameters in the zonal routine, the zones created are essentially of three types: 1) inviscid zones, 2) viscous zones with clustering on one face of the zone for wing or fuselage surfaces, and 3) viscous zones with clustering on two adjacent faces of the zone for the wing/fuselage juncture. Figure 4 shows the actual zoned grids about the modified F-16A.

The total number of grid points is approximately 270,000. The inviscid zones away from the geometry have as few as 3000 grid points, whereas the viscous grids contain about 28,000 grid points. The colors were used to distinguish the dif-

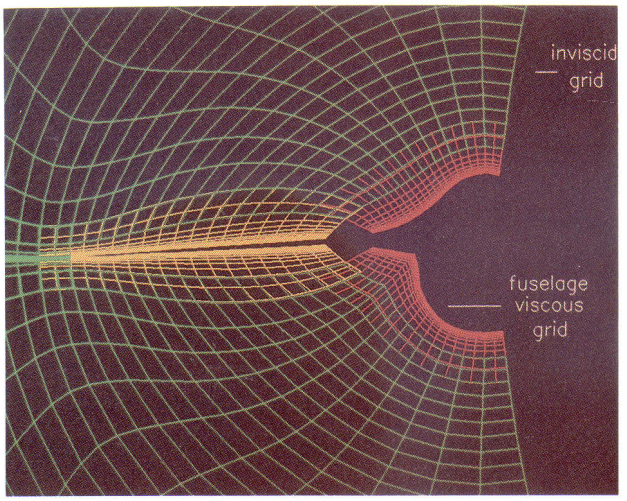


Fig. 5 Cross section of the fuselage/wing zonal grids and surface grid of zone 1.

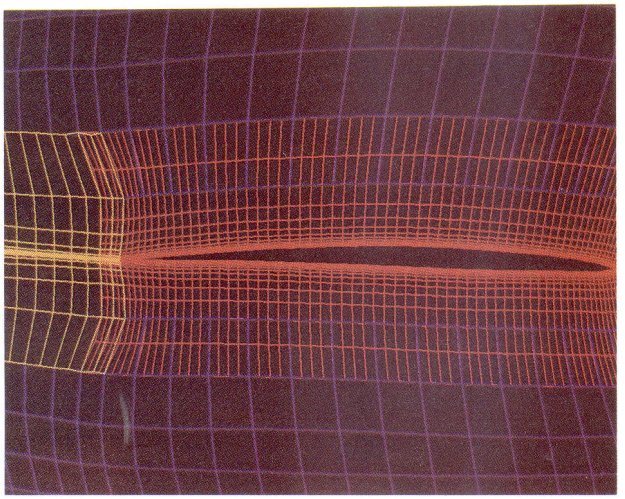

Fig. 6 Cross section of the wing-wake zonal grids.

ferent zones. The forward fuselage grid (red), and the mid-fuselage grid (yellow), although coarse in the streamwise and wraparound directions, are clustered in the normal direction. The wing grid (dark blue), however, is clustered in the normal, or wraparound, direction and is fine in the other two directions. The cyan (greenish-blue) grid, inboard of the wing, and the magenta grid describe the wing/fuselage and wake/wing/fuselage regions, respectively, with clustering on both surfaces. The cyan grid downstream of the wing, and the red grid outboard of the wing tip also can be seen to be clustered not only near the surfaces of the wing but across the wing planform plane.

Figure 5 shows a cross section of the fuselage and wing sections. The red grid demonstrates the fine clustering in the normal direction about the fuselage, and the yellow grids above and below the wing demonstrate the viscous clustering for the wing surfaces. The red clustered grid just outboard of the wing tip, as mentioned before, is to capture the vortex action occurring from the wing tip. The outer green coarse grids represent the inviscid zones above and below the wing. Figure 6 shows a cross section of the wing. The red grids show the clustering normal to the wing, and the yellow grid shows the clustering across the wing wake. The blue grid indicates the outer coarse grid, and the overlapping with the clustered grids can be seen. For the flow conditions of $M_\infty = 0.9$ and $\alpha = 4.12$ deg, this viscous clustering yields an average $y^+$ value, for the first point off the body, of $< 10$.

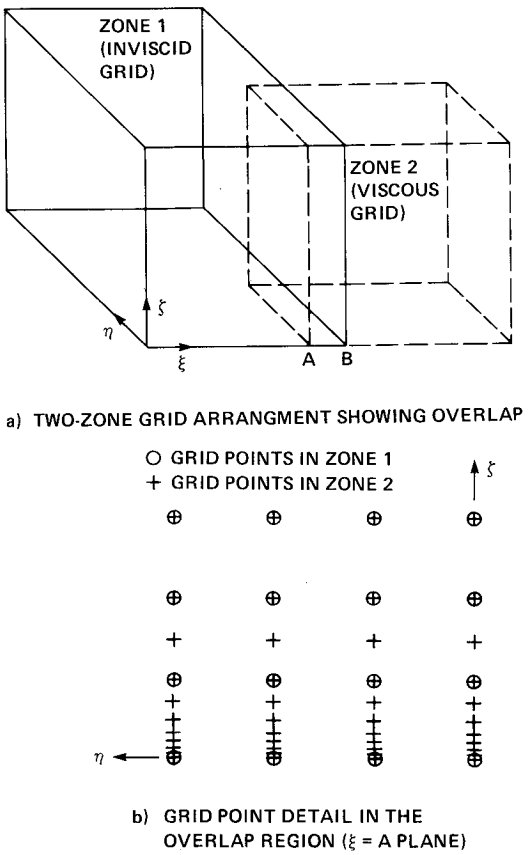


Fig. 7 Two-zone overlapping scheme: a) grid-point detail in the overlap region ($\xi = A$ plane); b) two-zone grid arrangements showing overlap.

### Transfer of Boundary Conditions

Communication between the blocks is achieved by means of an interpolation procedure. First of all, the grid zones are carefully (but automatically) constructed so as to overlap by a specific number of cells (usually one or two). Then, information required at the edge of one zone is interpolated from the interior of another zone. This situation is illustrated in Fig. 7. In this hypothetical case, grid zone 1 is an inviscid grid that interfaces with grid zone 2, a highly stretched viscous grid (see Fig. 7a). The idea is to obtain flowfield information from the interior of zone 1 and use it to satisfy the proper conditions on the $\xi = A$ plane of zone 2. An expanded view of this $\xi = A$ interface plane is shown in Fig. 7b. Note that the points from both grid zones are shown and that the grid points from grid zone 1 are represented as a subset of the grid zone 2 points. In this case, a series of one-dimensional linear interpolations is used in the $\zeta$ direction. If fine grid points also exist between the coarse grid points in the $\eta$ direction, then interpolation is needed in the $\eta$ direction as well.

The process of interpolating information back from zone 2 to zone 1, which is required for the $\xi = B$ interface plane, is even simpler than that in the first case. This is because the interpolation becomes simple "injection"; that is, even though interpolation is carried out, the end result of this operation is the straight transfer of values from zone 2 to zone 1 without interpolation errors. The interpolation process is automated to the extent that only the two planes involved in the interpolation, the base and target planes, need to be defined.

## Results

The case computed was for flow conditions of $M_\infty = 0.9$, $\alpha = 4.12$ deg, and a Reynolds number of 4.5 million based on root chord. Figure 8 indicates the pressure distribution compared with experiment for different spanwise stations and along the fuselage centerline.[26] The data points designated by

the upward- and downward-pointing triangles identify the experimental pressure distributions for the upper and lower surfaces of the wing, respectively. The solid line indicates the numerical computations. At the leading edge of the wing, the computations tend to underpredict the pressure coefficient. This, in fact, occurs across the entire wing, as will be evidenced from the other figures. This underprediction is due to the lack of resolution at the leading edge of the wing. The lower surface prediction is good, and the upper-surface agreement up to about 40% of chord is fair. The trailing-edge prediction is also good. The strong shock that the experiment indicates at about 73% of chord is not well resolved. The computation does show that the flow is supersonic and that it goes subsonic at about the 80% chord location. Failure to pick up the shock at this spanwise location may also be due to insufficient grid resolution in the streamwise direction. There are 60 points on the wing in the streamwise direction. As we proceed outboard, the resolution improves, owing to the tapering of the F-16A wing. For a spanwise location of $\eta = 0.59$, the upper-surface comparison is fair for the 30-40% of chord, with the leading-edge pressure again underpredicted and the shock not picked up by the computation. However, at the trailing-edge region, the computations match the experimental values very well.

At a spanwise location of $\eta = 0.71$, the grid resolution has improved, and the development of the shock can be clearly seen. The lower- and upper-surface pressures match fairly well over most of the chord. The location of the shock with the computations is off by about 5-10%; however, the flow calculations capture the peak pressure of the shock very well. For a spanwise location of $\eta = 0.84$, the prediction is again fair on the lower surface. The upper-surface comparison is fair also, with the peak pressure at the shock underpredicted. However, the pressure after the shock and the shock location are in good agreement.

Along the bottom of Fig. 8 is shown the $C_p$ distribution along the centerline at the top of the fuselage. The computations compare favorably with experiment up to the beginning of the canopy. The expansion region is underpredicted by computations, but this is due to insufficient grid resolution. Also, the recompression region is not picked up by the computations, but downstream the agreement is good. The last few experimental data points reflect the tail-assembly influence, which was not simulated in the computation.

This case required about 3000 iterations (15 h) for a three-order-of-magnitude drop in the L2 norm of the residual. The code was run using a single processor on the NASA Ames Cray XMP/48. The viscous blocks tend to converge faster than the inviscid ones. About 2000-2500 iterations (10-12.5 h) are required in the viscous blocks except for zone 2. Zone 2 (wing/fuselage junction region) had to be run at a lower time-step for stability reasons. At higher time-steps, stability problems were encountered at the interface between zone 2 and the zone directly above it.

In an effort to pick up the shock that was indicated by experiment ($\eta = 0.45$, 0.59) and that the computations failed to pick up, twice as many grid points were included in the streamwise direction on the wing. Figure 9 shows the comparisons of the experimental data and the computations with the old and new wing grids. TNSDOB indicates the new wing grid, which has twice as many points in the streamwise direction as the old wing grid. At $\eta = 0.45$, the leading-edge pressure is slightly improved. At about 70% of chord, the development of the shock can be seen. At $\eta = 0.59$ of span location, the shock can be seen to be developing at about the correct position, as indicated by the experimental results. The spanwise location of $\eta = 0.71$ and 0.84 exhibit the same trend near the shock location, that is, a sharper shock development. This result seems to indicate that the grid resolution is a primary reason for the lack of a shock structure at the inboard locations of the wing for the initial grid. It should be mentioned that as a result of the zonal implementation in this code, doubling the grid

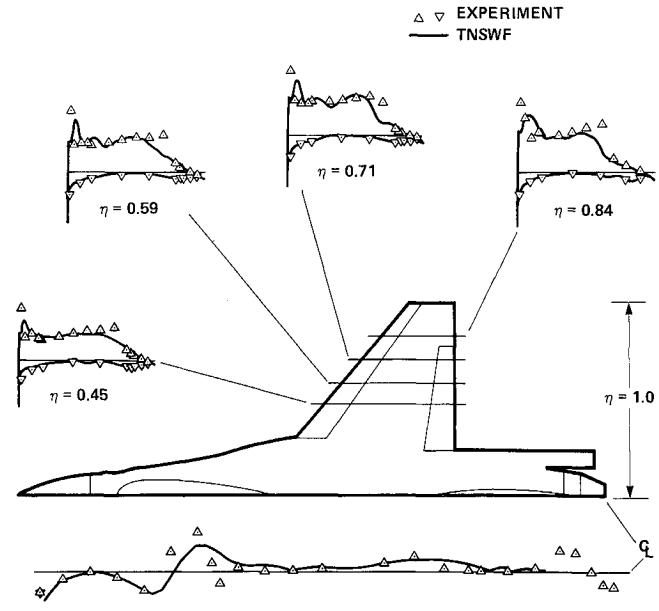


**Fig. 8 Comparisons of wing/fuselage pressure coefficients: $M_\infty = 0.9$, $\alpha = 4.12$ deg.**

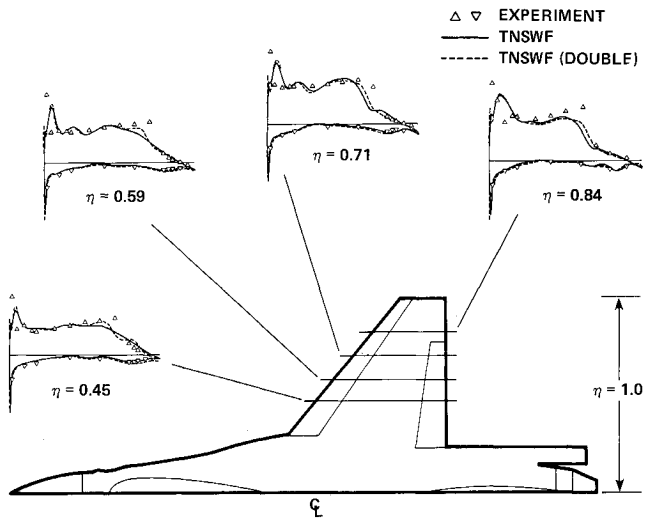


**Fig. 9 Comparisons of wing/fuselage pressure coefficients with refined grid.**

simply required a change in one parameter. In general, to change the dimensions of any grid is a trivial procedure.

Figure 10 shows pressure contours for this transonic case. The stagnation region and the acceleration of the flow over the canopy can be seen. The low-pressure region near the leading edge of the wing can also be seen, with the low-pressure region more evident near the wing tip. Also near the wing tip region, large gradients of pressure can be seen at about 70-75% of chord. Note also how the pressure contours are continuous from the wing surface zone across the fuselage surface zones. The continuity of the pressure contours can also be seen from the fuselage/canopy zone to the zone containing the rest of the fuselage downstream of the canopy.

Figure 11 shows an expanded view of the wing planform region with pressure contours. The large gradients of flow can be more easily visualized at the leading edge of the wing and near mid-chord (close to the tip of the wing), where the normal shock occurs. Concern was expressed because of the high pressure values at the strake region. The pressure values are

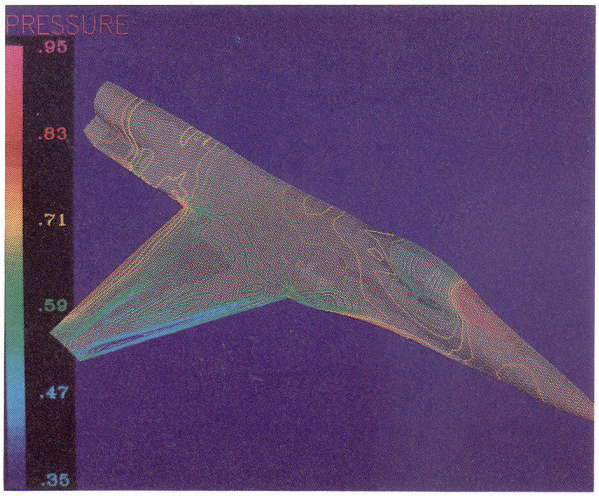


Fig. 10 Pressure contours over the F-16A.

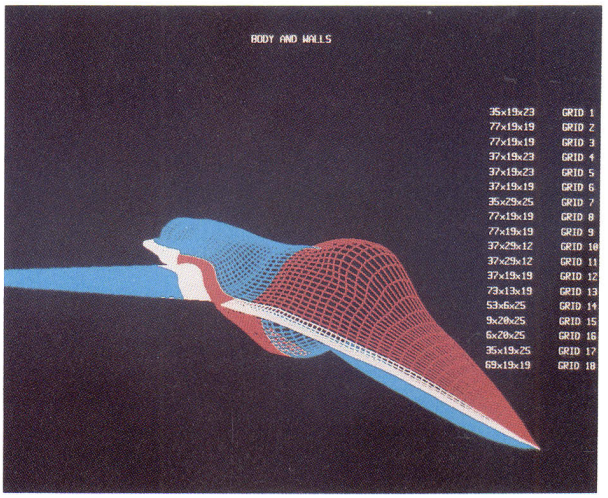


Fig. 12 Eighteen-zone version.

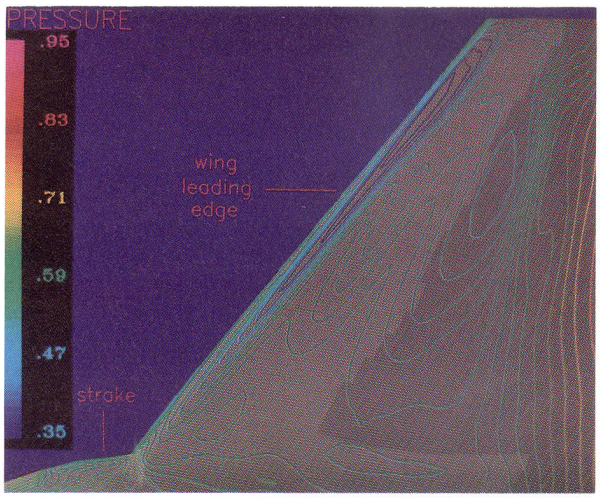


Fig. 11 Expanded view of pressure contours on wing/strake region.

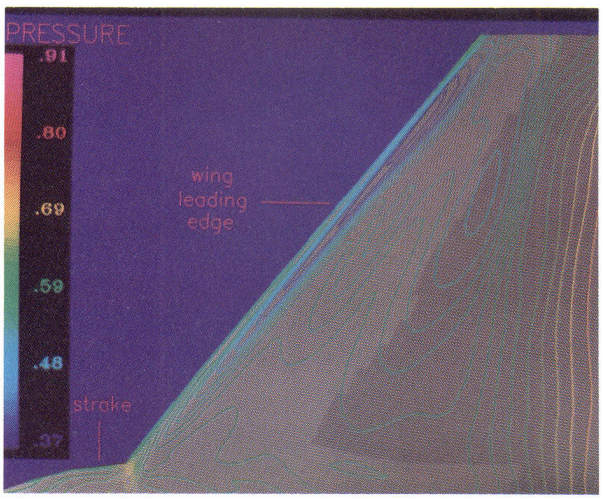


Fig. 13 Expanded view of pressure contours on wing/strake region.

not far from the values indicated after the normal shock region, that is, values in the yellow range of the pressure map. It is believed that this is due to the insufficient grid resolution in the wraparound direction in the strake region.

In order to verify this, two more refined zones were added to the current zonal topology in the vicinity of the strake leading edge. This modification required minor recoding. Figure 12 shows the 18-zone version and the grid dimensions. The new zones along the strake region are high-lighted in white. The power of the zonal method is that any number of grids can be implemented in regions where more resolution is required. Figure 13 shows an expanded view of the pressure contours on the wing for the 18-zone calculation. As expected, the pressure contours on the wing compare favorably with those of the previous computation. However, the pressure values seem to be lower along the strake relative to the previous computation with 16 zones; that is, there are more values in the green range of the pressure map as we proceed upstream along the strake. Again, a lack of grid resolution seems to have caused the unreasonable pressure values on the strake region. With the zonal procedure, it is a simple matter to resolve inadequate grid resolution.

Figure 14 shows a contour map of the Mach values for the wing/fuselage zones. This body-parallel plane occurs about 13 points above the body. At this location, the flow may still be in the viscous boundary layer, especially downstream near the trailing edge of the wing. However, the double shock pattern can be seen, with a peak Mach number of 1.45 at the leading edge of the wing, and a subsequent deceleration to a Mach number of about 1.2. This is followed by another shock at about 70% of local chord. The strong leading-edge shock is responsible for a separation bubble at the leading edge near the tip.

Figure 15 is an expanded view of the particle traces near the wing tip, where the strong shocks occur. From the leading edge, particles are released every three stations downstream for five spanwise stations near the wing tip. Inboard of this region, particles were released, but no interesting separation patterns occur for this transonic case. These particles are constrained to stay in the body-parallel plane, which is one point off the surface. The separation line is clearly visible at the leading edge; it occurs because of the strong shock at this location. Reattachment occurs very shortly downstream, showing a long (spanwise) but short (streamwise) separation bubble. The flow remains attached very close to the trailing edge of the wing, where it again separates. This latter separation is due to the adverse pressure gradient at the trailing edge of the wing and not to the secondary shock that occurs slightly uptream of this separation.

A $C_L$ vs $\alpha$ curve is displayed in Fig. 16, for an $M_\infty = 0.9$. The squares and triangles designate the experimental data and the computations, respectively. At an $\alpha = 1.69$ deg, we are in agreement with the experimental $C_L - \alpha$ curve; however, it would be expected that the computations would have lower lift owing to the lack of a tail assembly. As we increase the $\alpha$ to 4 and 6 deg, the underprediction of lift seems to increase from

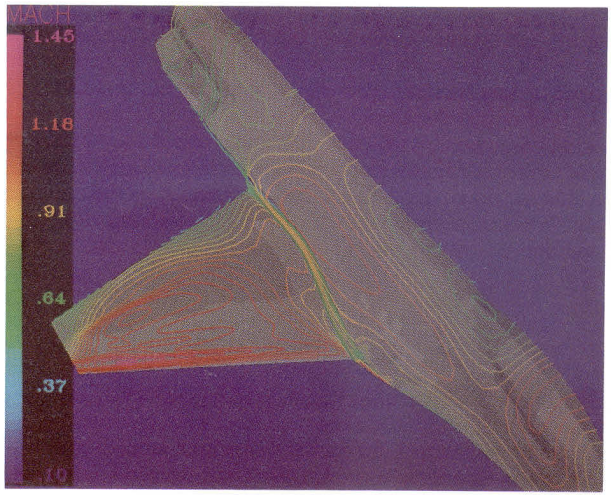


Fig. 14 Mach contours over the F-16A.

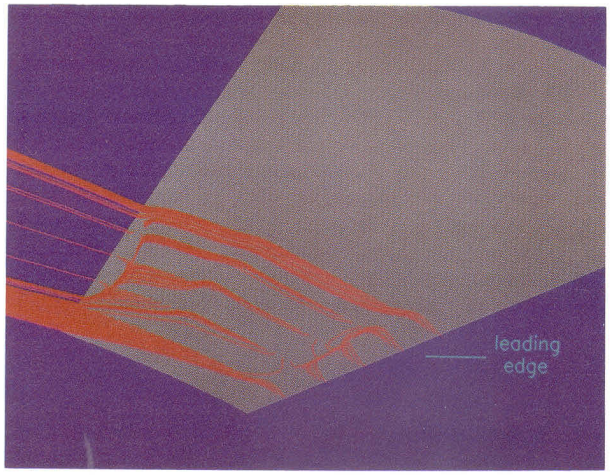


Fig. 15 Particle traces over expanded view of wing surface.

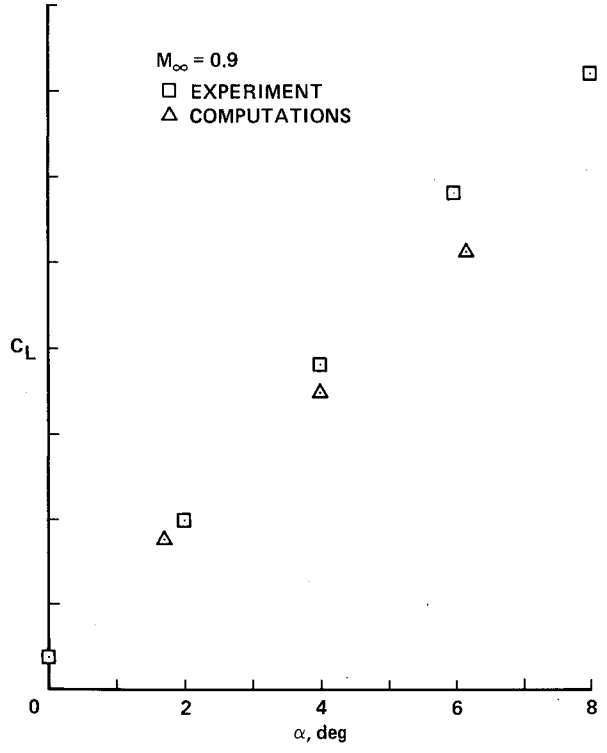


Fig. 16 $C_L$ vs $\alpha$ curve; $M_\infty = 0.9$.

the 4- to the 6-deg case. The computations may not be accurately predicting the nonlinear lift generated by the strake, which would increase the lift at the higher angles of attack, owing to the lack of grid resolution in the strake region. Also, the lack of grid resolution in the streamwise direction on the wing underpredicts the magnitude, as well as the extent, of the supersonic region on the upper surface of the wing. This would also result in less lift than the experimental value. Lastly, the influence of the faired-over inlet on the lift is still uncertain. Overall, the computations compare well with experiment.

## Conclusions

A new code, TNSWF, has been developed to compute the transonic viscous flow over a complicated fighter-like configuration. The TNSWF code uses a zonal approach, which allows appropriate clustering on all surfaces, a task extremely difficult for a single grid. The thin-layer Navier-Stokes equations are solved in the viscous regions, and the Euler equations are solved in the inviscid regions. It also allows for easy modification to increase the number of zones or refine existing zones for additional grid resolution where it is needed. Computations for a transonic turbulent case require about 3000 iterations, or about 15 h of CPU time on the current NASA-Ames computer. Pressure distributions along the top of the fuselage centerline and at various span stations on the wing compare favorably with those of experiment. A first of a kind $C_L$ vs $\alpha$ curve for the modified F-16A geometry has been generated by solving the thin-layer Reynolds-averaged Navier-Stokes equations and compares well with experiment. With the successful implementation of this code, numerical simulation of transonic viscous flow over complicated fighter-like configurations may now be attempted.

## Acknowledgments

The authors would like to acknowledge the work of Jason Williams, who is instrumental to the TNS project and for the color graphics contained in this paper.

## References

[1]Kutler, P., "A Perspective of Theoretical and Applied Computational Fluid Dynamics," AIAA Paper 83-0037, 1983.

[2]Ballhaus, W. F., "Supercomputing in Aerodynamics," presented at the Conference on Frontiers of Supercomputing, Los Alamos, NM, 1983.

[3]Cosentino, G. B. and Holst, T. L., "Numerical Optimization Design of Advanced Transonic Wing Configurations," AIAA Paper 85-0424, 1985.

[4]Holst, T. L., Tannehill, J. C., and Rakich, J. V., "Numerical Computation of Viscous Blunt Body Flows with a Planar Impinging Shock," NASA SP-347, 1975, pp. 1457-1471.

[5]Hung, C. M., "Numerical Solution of Supersonic Laminar Flow over an Inclined Body of Revolution," AIAA Paper 79-1547, 1979.

[6]Hung, C. M., "Impingement of an Oblique Shock Wave on a Cylinder," AIAA Paper 82-0025, 1982.

[7]Shang, J. S., "Numerical Simulation of Wing-Fuselage Aerodynamic Interaction," AIAA Paper 83-0225, 1983.

[8]Pulliam T. H. and Steger J. L., "Implicit Finite Difference Simulations of Three-Dimensional Compressible Flow," AIAA Paper 78-10, 1978.

[9]Deiwert, G. S. and Rothmund, H., "Three-Dimensional Flow over a Conical Afterbody Containing a Centered Propulsive Jet: A Numerical Simulation," AIAA Paper 83-1709, July 1983.

[10]Deiwert, G. S., Andrew, A. E., and Nakahasi, K., "Theoretical Analysis of Aircraft Afterbody Flow," AIAA Paper 84-1524, June 1984.

[11]Fujii, K. and Kutler, P., "Numerical Simulation of the Viscous Flow Fields over Three-Dimensional Complicated Geometries," AIAA Paper 83-1098, 1983.

[12]Mansour, N. N., "Numerical Simulation of the Tip Vortex Off a Low-Aspect Ratio Wing at Transonic Speed," AIAA Paper 84-0522, 1984.

[13]Chapman, D. R., "Computational Aerodynamics: Review and Outlook," *AIAA Journal*, Vol. 17, Dec. 1979, pp. 1293-1313.

[14]Atta, E. H., "Component-Adaptive Grid Interfacing," AIAA Paper 81-0382, 1981.

[15]Atta, E. H. and Vadyak, J. A., "Grid Interfacing Zonal Algorithm for Three-Dimensional Transonic Flows about Aircraft Configurations," AIAA Paper 82-1017, 1982.

[16]Hessenius, K. A. and Pulliam, T. H., "A Zonal Approach to Solution of the Euler Equations," AIAA Paper 82-0969, 1982.

[17]Rai, M. M., "A Conservative Treatment of Zonal Boundaries for Euler Calculations," AIAA Paper 84-0164, 1984.

[18]Chaderjian, N. M. and Steger, J. L., "A Zonal Approach for the Steady Transonic Simulation of Inviscid Rotational Flow," AIAA Paper 83-1927, 1983.

[19]Holst, T. L., Kaynak, U., Gundy, K. L., Thomas, S. D., and Flores, J., "Numerical Solution of Transonic Wing Flows Using An Euler/Navier-Stokes Zonal Approach," AIAA Paper 85-1640, 1985.

[20]Flores, J., Holst, T. L., Kaynak, U., Gundy, K., and Thomas, S. D., "Transonic Navier-Stokes Wing Solution Using a Zonal Approach: Part 1. Solution Methodology and Code Validation," AGARD Paper 30A, 1986.

[21]Flores, J., "Convergence Acceleration for a Three-Dimensional Euler/Navier-Stokes Zonal Approach," AIAA Paper 85-1495, 1985.

[22]Kaynak, U., Cantwell, B. J., and Holst, T. L., "Numerical Simulation of Transonic Separated Flows over Low-Aspect-Ratio Wings," AIAA Paper 86-0508, 1986.

[23]Eberle, A., "Euler Solution For a Complete Fighter Aircraft Configuration at Sub- and Supersonic Speed," AGARD Paper 17, 1986.

[24]Karman, S. L., Steinbrenner, J. P., Kisielewski, K. M., "Analysis of the F-16 Flow Field by a Block Grid Euler Approach," AGARD Paper 18, 1986.

[25]Sorenson, R. L., "Three-Dimensional Elliptic Grid Generation about Fighter Aircraft for Finite-Difference Solutions," to be published as a NASA TM.

[26]Reue, G. L., Doberenz, M. E., and Wilkins, D. D., "Component Aerodynamic Load from 1/9-Scale F-16A Loads Model," General Dynamics Rept. 16PR316, Fort Worth, TX, May 1976.

**Color reproduction courtesy of NASA Ames Research Center.**